HST Snapshot Survey of 3CR Quasars: The Data 1

Matthew D. Lehnert ^{2,3} , George K. Miley ² , William B. Sparks ⁴ , Stefi A. Baum ⁴ , John
Biretta ⁴ , Daniel Golombek ⁴ , Sigrid de Koff ^{2,4} , Ferdinando D. Macchetto ^{4,5} , and Patrick J.
$ m McCarthy^6$

Received; ac	$ccepted \dots \dots \dots$
--------------	-----------------------------

¹Based on observations with the NASA/ESA *Hubble Space Telescope*, obtained at the Space Telescope Science Institute, which is operated by the Association of Universities for Research in Astronomy, Inc., under NASA contract NAS5-26555.

 $^{^2 \}mathrm{Sterrewacht}$ Leiden, Postbus 9513, 2300 RA Leiden, The Netherlands

³Current address: Max-Planck-Institut für extraterrestrische Physik (MPE), Postfach 1603, D-85740 Garching, Germany, mlehnert@mpe.mpg.de

⁴STScI, 3700 San Martin Dr., Baltimore, MD 21218

⁵Affiliated with the Space Science Department, ESA

⁶Observatories of the Carnegie Institution, Pasadena, CA

ABSTRACT

We present images taken with the Wide Field Planetary Camera (WFPC-2) on the Hubble Space Telescope of 43 quasars selected from the 3CR radio catalog. The redshift range of the targets is large $-0.3 \leq z \leq 2$ and allows us to probe the nature of quasar hosts from about 20% to 80% of the age of the universe. These data were taken in the course of a large program that imaged 267 3CR radio galaxies and quasars using the HST in "snapshot" mode. Each quasar was centered on the Planetary Camera (PC1) and was imaged through the F702W filter (bandpass similar to Cousins R). Typical integration times were 5 and 10 minutes. For each quasar, we attempted to judge the contribution of the host galaxy to the total light from the quasar in two ways. The first method was to compare the radial light distributions of the quasars with that of both model point spread function and an empirical PSF constructed by summing individual observations of standard stars. Second, to provide morphological information we attempted to remove the contribution of the quasar nucleus from the extended emission by subtracting a point-spread-function constructed from observations of standard stars. This second method proved to be more sensitive in detecting marginally extended emission.

Our analysis suggests that the quasar fuzz contributes from <5% to nearly 100% in the most extreme case (about 20% being typical) of the total light from the quasar, with 16 of the quasars ($\sim 40\%$) being unresolved according to the analysis of their light profiles (with only 7 being considered unresolved determined by PSF subtraction of the quasar images). The magnitudes of the hosts range from about 18 to >21 in the F702W filter and the sizes are typically 1 to 2 arc seconds at a limiting surface brightness of $\sim 21-22~\mathrm{m}_{F702W}~\mathrm{arcsec}^{-2}$. Comparisons with the few ground-based images that are available of these sources suggest good overall morphological agreement with the HST images. The 0.1" resolution of the HST PC combination reveals a wide variety of structures in the host galaxies of these quasars. Most of the host galaxies show twisted, asymmetric, or distorted isophotes. About 1/4 of the quasar hosts have close (within a few arc seconds) companions seen in projection and about 1/10 show obvious signs of tidal interactions with a close companion. Finally, using radio images available from the literature, we find that in many of the resolved sources there is a correspondence between the radio and optical morphologies. We find that these sources exhibit a tendency for the principal axes of the radio and optical emission to align similar but perhaps weaker than that observed for radio galaxies. This correspondence also suggests that our methodology for removing the point source contribution from the resolved emission is sound. A more complete analysis of these data and new HST snapshot data will be presented in subsequent papers.

Subject headings: Galaxies: evolution — galaxies: jets — quasars: host galaxies — radio continuum: galaxies

1. Introduction

Observations of radio-loud quasars are important for investigating some of the most interesting and fundamental problems of contemporary astrophysics. The foremost of these is the investigation of causes of the "extinction" of luminous quasars. The space density of luminous quasars has declined by about 3 orders-of magnitude from the epoch z=2-3 to the present (e.g., Hartwick & Schade 1989). What processes led to the such a dramatic decrease in co-moving space density? Are these processes related to their galactic and/or cluster scale environments? The answers to these questions will be important in furthering our understanding galaxy evolution.

Studies of the environments of quasars can also provide insight into the AGN phenomenon in general. Of contemporary interest is the relationship between quasars and radio galaxies. A variety of schemes have been proposed to link quasars and radio galaxies through differences in their environments, viewing angle, or evolutionary state (e.g., Norman & Miley 1984; Barthel 1989; Neff & Hutchings 1990). In particular, the "viewing angle" scheme of Barthel (in which radio-loud quasars and radio galaxies are drawn from the same parent population but viewed preferentially at small or large angles, respectively, to the radio axis) predicts that the luminosity and color of the quasar fuzz should be identical to those of the radio galaxies at similar radio powers and redshifts (as do some of the evolutionary unification schemes). Also, radio galaxies at high redshifts ($z \ge 0.6$) exhibit the so-called "alignment effect" (McCarthy et al. 1987; Chambers et al. 1987) namely that the radio, and the rest-frame UV and optical axes are all roughly co-linear. If indeed quasars and radio galaxies are objects differentiated only by viewing angle, then quasars might also be expected to exhibit such an alignment effect over the same redshift range as the radio galaxies.

Investigating the above problems with ground-based data has been hampered by the inability of separating marginally extended "fuzz" from the "blinding" light of the quasar nucleus. But despite these difficulties, limited information about the properties of the host galaxies of quasars spanning a range of redshifts and radio properties has been obtained (see e.g., Hutchings, Crampton, & Campbell 1984; Smith et al. 1986; Stockton & MacKenty 1987; Veron-Cetty & Woltjer 1990; Heckman et al. 1991).

The Hubble Space Telescope is well-suited for investigating quasar host galaxies. Because of its high spatial resolution, imaging with the HST allows us to remove the contribution of the quasar nucleus and investigate the properties of the host galaxies on scales of 0.1 to a few kpc, depending on the redshift of the source. This was one of the reasons that motivated us to undertake a "snapshot survey" of sources in the 3CR catalogue. The "snapshot" mode of observing, in which gaps in the primary HST schedule are filled in with short integrations of selected targets, greatly enhances the overall efficiency of the HST and

is well-suited to observing large samples of objects. The results presented here should be compared and contrasted with recent HST results by other groups. Images of low/modest redshift quasars obtained with the WFPC-2 on HST show a wide variety of host galaxy morphologies including elliptical and spiral systems as well as highly disturbed, galaxies which may be interacting with and/or accreting close companions (Bahcall et al. 1995a,b; Disney et al. 1995; Hutchings & Morris 1995; Hooper et al. 1997).

The 3CR data set allows the properties of matched samples of radio-loud quasars and radio galaxies to be compared and should ultimately allow us to investigate the properties of "fuzz" over a wide range of redshifts $(0.3 \leq z \leq 2)$, radio luminosities (log $P_{178MHz} \sim 10^{27}$ to $10^{29.3}$ W Hz⁻¹) and radio types (e.g., lobe-dominated to core-dominated). Since low-frequency radio emission from radio-loud AGN is thought to be emitted isotropically, the low-frequency selection of the 3CR (178 MHz) implies that it is relatively unbiased by anisotropic emission (whether it is due to relativistic beaming, emission from an optically thick accretion disk, or due to an obscuring torus), thus the 3CR is particularly well suited for investigating the relationship between radio galaxies and quasars. Here we present and describe the image analysis and data reduction for 43 quasars from this "3CR snapshot survey". Other papers in this series have described the properties of the radio galaxies (de Koff et al. 1996; Baum et al. 1999; McCarthy et al. 1997) and future work will compare matched samples of radio galaxies and quasars over a wide range of redshifts.

2. Sample Selection

To select objects for the snapshot survey, we used the revised 3CR sample as defined by Bennett (1962a,b), having selection constraints of (i) flux density at 178 MHz, S(178) > 9 Jy, (ii) declination $> 5^{\circ}$, and (iii) galactic latitude, $|b| > 10^{\circ}$. All of the sources have been optically identified and have measured redshifts (Spinrad et al. 1985; Djorgovski et al. 1988). In this paper, we report on the properties of the quasars observed during the snapshot survey of a total of 267 3CR sources. The classification of these sources as quasars are based on the compilations of Spinrad et al. (1985) and Djorgovski et al. (1988). Of the total of 53 quasars listed in Spinrad et al. (1985), we have observed 41 (3C 179 and 3C 279, which we have observed, were not listed in the Spinrad et al. quasar identifications). Inevitable scheduling constraints and conflicts with other observing programs accounts for the 12 3CR quasars that were not imaged as a part of this program. Table 1 gives a summary of the observations.

3. Characteristics of the Observed Sample

The characteristics of the observed sample of quasars are provided in Table 2 and summarized graphically in Figures 1 through 3. The redshift distribution of the observed sample is fairly flat and ranges from 0.3 to about 2.1 (Table 2 and Fig. 1) and is broadly similar to that of the entire sample of 3CR quasars, the major difference is that a few of the lowest redshift quasars are excluded.

Adopting a cosmology with a Hubble constant of $H_0 = 75 \text{ km s}^{-1} \text{ Mpc}^{-1}$ and a deceleration parameter of q_0 =0.5 and using the 178 MHz radio fluxes of the sample as listed in Spinrad et al. (1985), the radio (178 MHz) power distribution of the observed sample lies in the range log $P_{178MHz} = 27 - 29.3 \text{ W Hz}^{-1}$. The distribution has a strong peak at log $P_{178MHz} \approx 28.5 \text{ W Hz}^{-1}$ (Figure 2 and Table 2). Hence the observed quasars are amongst the most powerful known radio sources.

Within the sample, the radio emission from these sources also exhibit a wide variety of physical sizes. Again, adopting the cosmology of $H_0 = 75 \text{ km s}^{-1} \text{ Mpc}^{-1}$ and $q_0 = 0.5$ and measuring the largest angular size of the radio sources using radio maps available in the literature (see Table 2 and §7), shows that these sources range from compact, galaxy-sized radio sources (largest projected linear sizes $\leq 10 \text{ kpc}$) to cluster-scale sources with sizes of a few hundred kpc (Figure 2).

4. Observations and Pipeline Reduction

The observations were taken throughout HST Cycle 4 (early 1994 to mid 1995) and the integrations times ranged from 2 to 10 minutes, with 5 or 10 minutes with being typical (see Table 1). All the quasars were observed close to the center of the Planetary Camera (PC) and imaged through the F702W filter, whose bandpass corresponds approximately to that of the Cousins R filter. The camera/filter combination was chosen to give the maximum spatial and photometric sensitivity. The large width of the F702W filter bandpass means that every quasar image has some contribution to its brightness and morphology due to one or two prominent emission lines. From the shape of the system bandpass for the F702W filter available in the HST WFPC2 Instrument Handbook (1995), the prominent lines that contribute to the emission within the images and the redshift range over which they contribute are: $[OIII]\lambda5007$ (0.19 < z < 0.64), $H\beta$ (0.22 < z < 0.67), $[OII]\lambda3727$ (0.60 < z < 1.20), $MgII\lambda2798$ (1.13 < z < 1.93). Only 3C 9 has a redshift (z=2.012) that avoids having prominent emission lines within the bandpass of the F702W filter.

The images were reduced using the standard pipeline (see the HST Data Handbook,

Version 2, 1995). The standard pipeline includes bias subtraction, dark count correction, flat-field correction, and a determination of the absolute sensitivity. For those objects that had two or more individual exposures (see Table 1), the separate images were combined using the STSDAS task CRREJ. This task constructs an average of the input frames and iteratively removes highly deviant pixels from the average. For those quasars with only one exposure, we used the IRAF task "cosmicrays" to remove the effects of cosmic rays. This task detects pixels that have significantly different value than the surrounding pixels and replaces the deviant value with the average of the surrounding pixels. Weak cosmic rays that were missed using this technique were subsequently removed by fitting the background to the area immediately surrounding the suspected cosmic ray hit and using this new value as a substitute for the old value of the counts in the affected pixel.

The data were flux-calibrated using the inverse sensitivity for the F702W filter of 1.834 \times 10⁻¹⁸ ergs s⁻¹ cm⁻² Å⁻¹ dn⁻¹ and a zero point of 22.469 (Whitmore 1995). This puts the magnitudes on the "Vega system". To convert to the STMAG system, which assumes a flat spectral energy distribution and has a zero point of 23.231, 0.762 magnitudes should be subtracted from the magnitudes given here.

5. Image Reduction

5.1. PSFs and EEDs

One of the most important steps of the analysis is to quantify the amount of extended emission from these quasar images. We have attempted this using two methods. To do this we collected images of the standard stars used to calibrate the F702W filter that were near the dates of the observations. Unfortunately, there were only a few exposures (5) that were useful. These were then used in two ways. We constructed an empirical point-spread function (PSF) using these observations by adding up the individual exposures after they had been aligned to a common center. This empirical PSF was then compared with the model PSF constructed using the PSF modeling program, Tiny Tim. However, as we discuss below, the close agreement is limited to azimuthal averages – Tiny Tim does not reproduce the detailed two-dimensional structure of the PSF. Next, we measured the encircled energy diagrams (EEDs), defined as the fraction of the flux from a point source interior to a radius r, as a function of r. We then intercompared all the EEDs (including the PSF generated by Tiny Tim) taken through a given filter to determine the reproducibility of the EED. There was very good agreement between the shape of the EED from the sum of the observations of standard stars and that of the Tiny Tim PSF but insufficient data were available to perform this comparison for individual stars/PSFs taken with the F702W filter. Fortunately, we also carried out this analysis for another of the WFPC2 filters, F555W, in the course of another HST program (Lehnert et al. 1999). For this intercomparison, we used observations of approximately 20 stars. This intercomparison implies that we can robustly detect fuzz that contributes more than about 5% as much light as the quasar itself (within a radius of about 1.4 arcsec). This limit is consistent with the known temporal variations in the HST PSF due to effects like the gentle change in focus over times scales of months and shorter (orbital) time scale variations due to the so-called "breathing" of the telescope (see WFPC-2 Instrument Handbook). We have restricted ourselves to radii less than about 1.5 arc seconds due to the poorly understood large angle scattering which becomes important beyond a radius of about 2".

To quantify how much of the quasar light is extended, we compared the EEDs of each quasar to that of the PSF (both empirical and model, although it makes little difference which one is used). We accomplished this by scaling the PSF EED so that the total flux difference between the PSF EED and that of each quasar is zero inside a radius of 2 PC pixels (≈ 0.09) . The EED analysis is conservative in that the actual underlying fuzz will certainly have a finite non-zero central surface brightness. Therefore, this analysis provides a lower limit to that amount of extended flux coming from each quasar. Moreover, the choice of using a radius of 2 pixels was not arbitrary. Experimenting with the effect of scaling by the central pixel led to a much higher variation in the structure of each stellar EED compared to the EED of the model PSF. This variation is due to our limited ability in determining the exact location of the peak of emission and also due to the fact that the central point source never falls exactly in the center of one pixel. Enlarging the area overwhich the quasar and PSF are scaled greatly reduced the variation in the structure seen in the PSF by the EED analysis. However, selecting a large area leads to very limited sensitivity to extended emission and thus a radius of 2 pixels was chosen as the most suitable choice to maintain the sensitivity to mildly extended fuzz but also minimizing systematic problems. In addition, we limited the EED analysis to a radius ≤ 30 PC pixels (≈ 1.4 "). This mimizes the problem of the large angle scattering which may not be well represented in the empirical or model PSF but may contribute to the extended emission in the quasar images. Therefore, in Table 3, we quote the amount of extended emission as a fraction of the total quasar emission within a radius of 30 PC pixels (1.4"). In Figure 4, we show all of the profiles from the EED analysis.

The EED procedure assumes that the peak flux of the underlying galaxy is zero. Of course we know that this is a lower limit. To investigate how much flux we may miss in the course of such a procedure, we conducted the EED analysis for a small sample of 10 radio galaxies also observed as part of the snapshot survey. These galaxies were chosen to represent the full range of morphologies and (most importantly) central surface brightnesses seen in the data on radio galaxies (see de Koff et al. 1996; McCarthy et al. 1997). Although

the images reveal non-thermal nuclei in a few objects, none are as "PSF dominated" as any of the quasars. Under the assumption that radio galaxies are similar to quasar hosts in morphology and central surface brightness and that the central surface brightness observed are due to the underlying galaxies and not the AGNs, we determined the EED fluxes for the radio galaxies. These fluxes were smaller than the measured total fluxes by an amounts ranging from about 8% to 50% (with about 30% being the average) of the total extended light. We regard this as a reasonable underestimate of the quasar fluxes by the EED analysis.

5.2. PSF Subtraction

There are obvious limitations to using the EED analysis described above. The foremost of these is that it does not provide information on the morphology of the host galaxy. Also, it in fact only provides a lower limit on the amount of extended emission since we have assumed that the contribution to the fuzz from the central 0.03 \(\pi''\) is zero. To study the host galaxy morphology, it is necessary to first remove the contribution of the quasar nuclei from the images. Therefore to provide morphological information about the host galaxies, we next attempted subtraction of a scaled PSF from each of the quasar images. We used two different PSFs, a model of the HST PSF constructed using Tiny Tim and an empirical PSF constructed by averaging several images of standard stars. We would have preferred to construct a PSF using exposures of open clusters or of outer regions of globular clusters but no such images were available from Cycle 4 observations taken through the F702W filter. Also only a limited number of exposures of standard stars were available and some of the stellar images were far (up to about 300 pixels) from the center of the PC. If there were two or more images of the same standard taken at the same position close in time, the individual exposures were averaged. Images of different standards were then summed after being aligned to the nearest pixel. The model and empirical PSFs were scaled such that their peaks were about 5 - 15% of the highest valued pixel in the quasar image and iteratively subtracted until emission due to the diffraction of the secondary support become negligible or the flux in the central pixel of the quasar image was too small to be measured. During this procedure we noted the subtraction level where residual diffraction spikes were just above the background noise level. Also, we continued the subtraction until a negative image of the diffraction spikes appeared above the level of the noise. This procedure allowed us to estimate the uncertainty in the fraction of extended emission by observing the values where the diffraction spikes in the residual image became negative due to over-subtraction of the PSF or were still present due to under-subtraction.

The relatively subjective method described above allows us to parameterize the uncer-

tainty in the PSF subtraction procedure as a function of the total brightness of the quasar. We found that for most of the quasars, the uncertainty in the flux of the host relative to that of the total (quasar plus host) was about $\pm 7\%$. For about 20% of the sample (8 quasars), the uncertainty was larger, about $\pm 15\%$ of the total quasar flux. We used these estimates to categorize the quasars into three groups according to the uncertainties in the fluxes of the remnant hosts. The three categories correspond to $\sim \pm 0.2$, $\sim \pm 0.4$, and $\sim \pm 0.7$ magnitudes.

After conducting the subtraction process with both the model PSF and the empirical PSF for about 10 of the quasar images, we concluded that the model PSF was inadequate for PSF subtraction. There is an asymmetry in the intensity of the diffraction spikes within the PC point-spread-function. The diffraction spike along the positive direction of U3 axis (see HST WFPC2 Instrument Handbook 1995) and in a direction -45° relative to the U3 axis are more intense than those along the other two directions (the spike along the +U3 axis being the most intense). The model PSF does not characterize this asymmetry accurately. On the other hand, while the empirical PSF characterized this asymmetry well, because of the limited number of standard star exposures available, the empirical PSF only accurately characterized the PSF over a limited radius. Hence the empirical PSF was good for representing and removing the PSF structure from the quasars that did not have highly saturated nuclei. For the quasar images that appeared to be only mildly saturated a small residual sometimes was present along the brightest diffraction spike (the spike along the +U3 direction), \approx 1" from the nucleus and occupying a few pixels in diameter. This distinct residual was easily identifiable and removed using fits to the surrounding background. This correction needed to be applied to about 12 of the quasar images and those quasars are noted in Table 3. This residual removal was carried out mainly for cosmetic reasons. The residuals contained very little flux and since the residual was in every case well separated from the quasar host, it has only a small effect on the final host morphology. For four quasars (3C 205, 3C 279, 3C 351, and 3C 454.3) the nuclei were highly saturated and we do not present the results of the PSF subtraction due to their unreliability. Generally, since the exposure times for all the quasars were roughly the same, quasars with brighter nuclei were more difficult to determine reliable host morphologies and brightnesses through PSF subtraction.

After PSF subtraction, the images were rotated so that north is at the top of the frame and east is to the left. Then each images was smoothed with a 4×4 pixel median filter to remove the effects of "hot" pixels and residual cosmic rays, to emphasize low surface brightness features, and to reduce the additional noise in the final image due to the noise in the image of the empirical PSF used for subtraction. Contour plots of the final images are displayed in Figure 5 and 6.

We note that the relatively "clean" appearance of the contour plots is due to the way

in which they were constructed. PSF subtracting the images leads to an increase in the overall noise of the image near the quasar. After the image was smoothed by a 4×4 pixel median filter we then selected the lowest contour to be at about the 3σ noise level in the region affected by the PSF subtraction, but well away from the host galaxy. Therefore, the minimum level is relatively high compared to the noise level of the entire displayed image. Picking such a relatively high minimum contour level has the benefit of only showing morphological features that have a high certainty of being real and not artifacts of the PSF subtraction. As noted above, any additional "cleaning" of the images was strictly limited to the removal of the residual along the +U3 direction approximately 1" from the nucleus in the quasars as noted in Table 3. Even this procedure had only a marginal influence on the final displayed morphology. In addition, in the one case (3C 179.0) where we subtracted individually two images taken at different times, there was close morphological agreement between the two images of the host galaxy in spite of the rather dramatic change in the total magnitude of the nucleus.

5.3. On the Differences Between the EED Analysis and PSF Subtraction

As can be seen in Table 3, there are rather large differences between the amount of resolved fluxes estimated using the EED analysis and the PSF subtraction. These differences are not surprising. First and perhaps most importantly, the EED analysis is basically an integral process and thus it is sensitive to low signal-to-noise, smoothly distributed light, whereas the PSF subtraction analysis is inherently differential and highlights the very small scale features lost in the growth-curves. Second, the EED analysis will always underestimate the amount of resolved flux since it assumes that the fraction of host light in the unresolved core (central $\sim 0.1 \, \Box''$) is negligible and then scales the contribution of "fuzz" under this assumption. Thus one cannot simply measure the amount of flux from the central $\sim 0.1 \, \Box''$ to reconcile the estimates from the EED analysis with that from the PSF analysis. Moreover, it is known that as the focus of the HST changes, different parts of the PSF are affected in different ways (C. Burrows and M. McMaster, private communication). Therefore, using the diffraction spikes to gauge when to stop subtracting scaled PSFs from the image, may not give the proper subtraction of the flux from the nuclear region. This was clearly evident for some of the quasars where the flux would almost reach zero near the nucleus as emission from the diffraction spikes disappeared into the noise. Since there is some disagreement in the amount of resolved flux between the PSF subtraction and the EED analysis, in Figure 6, we provide images of the quasars that are not classified as extended by the EED analysis, but apparently have some extended flux in the PSF subtraction analysis. There are 8 such objects.

5.4. On the Consistency of Our Results with Other Investigations

Since it is difficult to ascertain robustly whether or not our procedure for determining to what extent the quasars images are extended, it is important to compare our results with those obtained by other investigators. Of course, this is challenging given the variety of individual circumstances (HST versus ground-based data, use of adoptive optics, different filters, optical versus IR images, etc) by which quasar hosts have been observed. Limiting ourselves to comparisons with other HST programs to image quasar hosts in the optical, we can say that we find broad consistency between the results presented here and those of other programs investigating the hosts of radio loud quasars. For example, Boyce, Disney, & Bleaken (1999) and Boyce et al. (1998), for small samples of low-z radio-loud and radioquiet quasars, found extended to total flux ratios of roughly ten to a few tens of percent for the radio-loud quasars in their studies which imply host magnitudes consistent with our results. At moderate redshifts, 0.4 < z < 0.5, in a study of radio loud and radio-quiet quasar hosts, Hooper, Impey, & Foltz (1997) again found extended to total flux ratios of roughly ten to a few tens of percent for their radio-loud subsample which also imply host magnitudes consistent with our results. At the high redshifts (z>1), in two small samples of radio-loud quasars, both Ridgway & Stockton (1997; which also included radio galaxies) and Lehnert et al. (1999) find similar host galaxy magnitudes as we find here for similarly high redshift quasars.

The broad agreement between the results of the study presented here and those of other studies of radio-loud quasars using the WFPC2, we are confident that our analysis is robust. However, this statement needs to be made more quantitative and we plan to make detailed comparisons between our results and those of other studies in subsequent papers.

6. The "Alignment Effect" for 3CR Quasars

The "Alignment Effect" in which the axes of the optical and radio emission roughly align is a well known effect observed in high redshift radio galaxies (Chambers et al. 1987; McCarthy et al. 1987). An interesting test of various schemes attempting to relate the properties of radio galaxies and quasars is to determine whether or not a sample of quasars also exhibits a similar alignment. To this end, we measured the position angles of the radio images from the literature as given in Table 2. These position angles were determined from the core of the radio emission along the position angle of the jet. If a jet was not obvious in the radio image used, we then measured the position angle of the highest surface brightness "hot spot" relative to the core. For the HST images, we measured the position angle by fitting a series of ellipses as a function of surface brightness using the STSDAS program "ellipse" of

the PSF subtracted, rotated and median smoothed quasar images. The position angle of the optical emission was taken to be the position angle at a surface brightness of $21.5~\rm m_{F702W}$ arcsec⁻² for all of the quasars. This value was chosen because it was the surface brightness that was bright enough so that the ellipses that were fitted to the data gave believable results with small uncertainties for all of the quasar images (i.e., the uncertainty in the ellipticity was <0.07 and the uncertainty in the PA was <20°). We present the measured radio and optical position angles in Tables 2 and 3 respectively and a histogram of the difference in the radio and optical position angles in Figure 7. Figure 7 shows a tendency for the difference between the position angle of the principal axes of the radio and optical emission to be less than 20° .

We present this result for two reasons. One of course is because this is an important result for schemes that attempt to unify quasars and radio galaxies based on viewing angle, evolution, or environment (e.g., Norman & Miley 1984; Barthel 1989; Neff & Hutchings 1990). Our main reason for presenting this result is that it lends support for our methodology for determining if the quasar image is resolved and if so, for determining the morphology of the underlying host galaxy. Of course it is important not to overstate this proposition. When comparing the "alignment" properties of radio galaxies and quasars one obviously needs to worry about projections (especially for the quasars), since the UV and radio are not likely to be perfectly aligned in three dimensions. In spite of this caveat, we would not expect to see any correspondence between the radio and optical if the morphology revealed through PSF subtraction happened by chance. However, we also note that there is a possible weakening of the alignment with redshift and this may be an indication of the difficulty in resolving high redshift hosts with short exposures through the WFPC2 (hence we urge some due caution in over interpreting our results). A more robust analysis of the importance of this result and a comparison of the strength of the "alignment effect" in quasars and radio galaxies will be presented in a subsequent paper.

7. Individual Source Descriptions

In this section, we shall describe the morphologies of the individual sources focusing on the following questions. Are there any artifacts in the images related to the PSF subtraction? What is the morphology of the extended emission (isophotal size, ellipticity, orientation)? Are there signs of interactions with nearby companions? How does the radio structure relate to the optical morphology of the host as seen in the HST data? We shall also discuss the positional offsets between the quasar nucleus and any nearby (in projection) companions seen in the contour plots and the magnitudes of these companions.

3C 9, z=2.012

3C 9 has the highest redshift of the quasars in our sample. A short (10 minute) ground-based U-band exposure of 3C 9 in Heckman et al. (1991) did not reveal any extended structure. Our HST observations do not detect extended flux.

3C 14, z=0.469

The image of this source is approximately round. At the faintest isophotes it is preferentially extended along PA \approx 120°. At higher isophotal levels, the orientation of the image is close to PA \approx 180°. There is a diffuse galaxy about 0.7" south and 2.6" west of the nucleus with a total magnitude of about $m_{F702W} \approx 23.2$. The radio source has a triple morphology and is extended along PA \approx -5° and 170° (Akujor et al. 1994) — very similar to the PA of the highest surface brightness extended optical emission.

3C 43, z=1.47

3C 43 is optically one of the most compact objects in our sample. The PSF subtracted image has a faint extension along PAs $\approx 30^{\circ}$ and 180°. Emission is extended to only about 1" down to a surface brightness of 22.9 m_{F702W} arcsec⁻². 3C 43 has a compact (LAS \sim 2.6") and complex radio structure (Sanghera et al. 1995; Akujor et al. 1991). This complex morphology makes a direct comparison between the optical and radio emission difficult, but it is interesting to note that the "U-like" structure seen in the faintest isophote to the north of the nucleus is roughly mimicked in the radio map of Sanghera et al. (1995). The most northern component of the complex radio structure has been identified as the nucleus by Spencer et al. (1991). If this is the case then the extended optical emission to the south of the optical nucleus is roughly aligned with the curved jet seen in the radio images of 3C 43 (e.g., Sanghera et al. 1995). There is a nearby (in projection) companion galaxy about 3" north and 0.2" east of the quasar nucleus with a total magnitude, m_{F702W} \approx 23.5. There is another galaxy just visible on the edge of the contour plot shown in Figure 5, which is almost certainly a foreground galaxy.

3C 47, z=0.425

3C 47 shows signs of interaction with a small galaxy approximately 1.7 arc seconds to the northeast of the nucleus. There is a second galaxy along this same direction approximately 3.5 arc seconds from the nucleus. These galaxies have total magnitudes of 21.6 m_{F702W} and 21.7 m_{F702W} respectively. The elongated, off-center (i.e., not centered on the nucleus) isophotes strongly suggest that the host galaxy is interacting with one or both of the nearby (perhaps only in projection) galaxies. The 5 GHz radio map of Bridle et al. (1994) show a core, jet, and two lobe morphology. The jet is at PA \approx 210° which corresponds closely with

a linear feature seen in the HST image presented in Figure 5.

3C 68.1, z=1.238

The HST data are consistent with a point source and thus we do not detect any extended flux around 3C 68.1.

3C 93, z=0.357

3C 93 possesses a host with a large angular size — approximately 3" in diameter (at a surface brightness of 22.9 m_{F702W} arcsec⁻²). The isophotes are approximately round, with the brighter isophotes being extended along the north south-direction and the faintest isophotes oriented along PA \approx 40°. The 1.5 and 8.4 GHz radio maps of Bogers et al. (1994) show a "core + double lobe" radio source with a relatively large angular size (\sim 41"). The radio source is oriented along PA \approx 45° and thus roughly coincident with the principal axis of the outer isophotes. The morphology of the host galaxy agrees well with the R-band image of 3C 93 presented in Hes, Barthel, and Fosbury (1996).

3C 138, z=0.759

3C 138 is a flattened system oriented preferentially along $PA\approx130^{\circ}$. The inner isophotes become irregular with extensions along $PA\approx70^{\circ}$ and along $PA\approx290^{\circ}$. 3C 138 is also a so-called compact steep spectrum (CSS) radio source. The high resolution radio map of Redong et al. (1991) shows a compact source whose linear and triplet structure is extended on scales of a few tenths of an arc second along $PA\approx70^{\circ}$. This axis of emission is similar to the extension of the isophotes on scales of a few tenths of an arc second seen in the optical image.

3C 147, z=0.545

The isophotes of 3C 147 are fairly flat in the high surface brightness regions and become rounder at fainter isophotal levels. The main axis of the optical emission is at PA \approx 55°. The galaxy is about 2" across down to about 22 m_{F702W} arcsec⁻². 3C 147 is also a well known compact steep spectrum radio source whose size is 0.5" and has a jet-like structure pointing out from the nucleus at PA \approx 240° (van Breugel et al. 1992). Moreover, there is a blob of emission 0.4" from the nucleus at PA \approx 25°. In the HST image, we also see two blobs of emission about 1.4" to the south of 3C 147. The total magnitude of these two blobs is about 21.7 m_{F702W}. There is also another bright galaxy visible 3.3" east of the nucleus. The total magnitude of this galaxy is 19.4 m_{F702W}.

$3C\ 154,\ z=0.580$

The HST data are consistent with a point source in the EED analysis. However, there

is evidence for extended emission from the PSF subtraction. In Figure 6, we show the morphology of this extended emission. The F702W image of 3C 154 extended by about 1.5" at a level down to a surface brightness of $22 \text{ m}_{F702W} \text{ arcsec}^{-2}$. Radio maps of 3C 154 show a classical core, double lobe morphology (e.g., Bogers et al. 1994). The source is oriented along PA \approx 100° and is large (LAS \sim 53"; Bogers et al. 1994). The position angle of the radio source corresponds to a faint extension in the HST image that reaches about 1.2" from the nucleus down to a surface brightness of $22 \text{ m}_{F702W} \text{ arcsec}^{-2}$.

$3C\ 175,\ z=0.768$

The HST image of 3C 175 is marginally resolved. The PSF subtracted image shows a complex morphology. The inner, brighter isophotes are oriented preferentially east-west. The fainter isophotes show a "plume" of emission to the south-east and south of the nucleus. This "plume" reaches about 2" from the nucleus (down to $22~\mathrm{m}_{F702W}~\mathrm{arcsec}^{-2}$). The radio source also has a "classical" radio structure of core and two radio lobes. This triple structure is oriented along PA \approx 240° (jet side). The size of the radio source is large — LAS \sim 56". In the optical image there is an extension in the isophotes along PA \approx 240°. There is no evidence from ground-based optical images of 3C 175 that it is resolved (Malkan 1984; Hes et al. 1996).

3C 179, z=0.856

The images of 3C 179 were reduced using a different method than the rest of the sample. Two 300 second images were taken of 3C 179 separated by a period of a month. Over that time, 3C 179 increased by about 0.5 magnitudes in brightness. We therefore PSF subtracted each image individually and, aligned and rotated both residual images and then averaged the two images. The magnitude and fraction of the extended emission was obtained by comparing the average quasar brightness with that of the average host brightness. Of course the fraction of extended to total flux was different in the two images.

The brightest isophotes of the fuzz are oriented preferentially in the east-west direction. There is a bright "knot" of emission about 0.8" from the nucleus along a $PA \approx 270^{\circ}$. The radio maps of Reid et al. (1995) show a complex morphology. The radio maps show a jet along $PA \approx 270^{\circ}$ and a double lobe morphology.

3C 181, z=1.382

The image of 3C 181 does not appear to be spatially resolved in these HST data.

3C 186, z=1.063

The image of 3C 186 is not resolved according to the EED analysis. However, the PSF

subtraction suggests that it might be resolved. We show the possible morphology of the host in Figure 6. The image of 3C 186 shows "fuzz" about 1.8" across down to a surface brightness of $22 \text{ m}_{F702W} \text{ arcsec}^{-2}$. There are two significant position angles of extended emission, PA \approx 30° and PA \approx 110°. There is a nearby (in projection) galaxy about 2.3" from the nucleus along PA=65°. The total magnitude of this nearby companion is m_{F702W} =22.2. The radio morphology is compact and is oriented along PA \approx 140° (Rendong et al. 1991; Spencer et al. 1991).

3C 190, z=1.195

The PSF subtracted image of 3C 190 reveals a complex morphology. The principal axis of the optical emission is along PA \approx 140°. There is a clump of emission approximately 0.8" to the east of the nucleus. The radio morphology of 3C 190 is compact (LAS \sim 3") and is linear having a chain of several hot spots (Spencer et al. 1991) along PA \approx 240°. In the HST image, we see a distortion in the isophotes along the PA of the radio structure.

3C 191, z=1.956

There is no evidence for a resolved component in 3C 191 according to the EED analysis, but PSF subtraction analysis suggests that it is resolved. The PSF subtracted image of 3C 191 reveals a complex morphology. The general orientation of the fuzz is along PA \approx 0° and \approx 200°. There is a "plume" of emission to the southeast of the nucleus along PA \sim 140°. The radio morphology is a core plus double lobe morphology with a principal axis of emission along PA \approx 165° (Ankujor et al. 1991).

3C 204, z=1.112

3C 204 has a relatively high percentage of extended to total emission (almost 50%). The host galaxy is a flat system ($e\sim0.25$) and its major axis is oriented preferentially along PA $\approx150^{\circ}$. The radio emission has a core, jet, double lobe morphology with the jet oriented along PA $\approx275^{\circ}$ (Reid et al. 1995). There appears to be a faint extension of emission along PA $\approx275^{\circ}$ in the HST image of the host galaxy. This "finger" of emission may be related to the radio jet seen in the radio image of Reid et al. (1995).

3C 205, z=1.534

The HST image of this quasar was saturated. No PSF subtraction or EED analysis was attempted.

$3C\ 207,\ z=0.684$

3C 207 does not appear to be extended in these HST data.

$3C\ 208,\ z=1.110$

3C 208 does not appear to be extended in these HST data.

3C 215, z=0.412

The optical counterpart of 3C 215 appears to have a flattened elliptical structure with its major axis oriented along PA \approx 135°. The 5 GHz radio image of Bridle et al. (1994) shows a complex structure with an inner region consisting of several high surface brightness knots of emission along an approximately east-west line, engulfed in a large, more diffuse emission oriented along PA \approx 150°. The radio emission is seen over a large scale, LAS \sim 1'. A ground-based V-band image presented by Hes et al. (1996) shows a similar morphology to the image presented here.

$3C\ 216,\ z=0.67$

The HST image of 3C 216 indicates that the host galaxy is an interacting system. The faint isophotes of the quasar fuzz are not centered on the quasar nucleus, but are offset to the northeast along PA \approx 30 — 45°. The nearby (in projection) galaxy is about 1.6" to the north of the nucleus and has a magnitude of 21.9. There is another brighter galaxy just off the edge of the contour plot presented here is about 4" to the east and 2.5" north of the nucleus. The total magnitude of this galaxy is $m_{F702W} \approx 20.4$. The 1.7 and 5 GHz radio images of Reid et al. (1995) show a compact radio source (LAS \sim 6") oriented along PA \approx 40°. Along this PA lies a radio "hotspot" about 1" from the nucleus. This hotspot is approximately coincident with the "plume" of optical emission we see in the HST image.

3C 220.2, z=1.157

3C 220.2 does not appear to be extended in these HST data.

3C 249.1, z=0.313

The HST image of 3C 249.1 is spectacular. The extended emission comprises about 70% of the total light from the quasar. A narrow-band HST image centered on $[OIII]\lambda 5007$ (Sparks, private comm.) shows that most of the emission to the east of the nucleus is probably [OIII] emission within the bandpass of the F702W filter (see also Stockton & MacKenty 1987). However, the comparison with the narrow-band [OIII] image suggests that much of the light from the inner parts of the nebula is likely to be continuum emission from the host galaxy. A 5 GHz radio image of Bridle et al. (1994) reveals a core, jet, double lobe morphology oriented preferentially along PA $\approx 100^{\circ}$.

3C 254, z=0.734

The EED analysis of 3C 254 shows no evidence for resolution, but the PSF subtraction indicates that it is probably resolved. The HST image of 3C 254 has a complex morphology. Its host galaxy is oriented approximately in the east-west direction. There are "plumes" of emission along $PA \approx 45^{\circ}$ and 285° . The second of these plumes corresponds to the direction of the most distant radio lobe seen in the 5 GHz radio map of Reid et al. (1995). This radio map reveals that 3C 254 has a double-lobed radio morphology with a central core.

$3C\ 263,\ z=0.646$

The host galaxy of 3C 263 appears to be a flat system (e \sim 0.3), with its major axis aligned along PA \approx 350°. There is a nearby galaxy in projection along the major axis of the galaxy (\approx 1.9" from the nucleus) with a magnitude of 22.2. There is also another nearby galaxy about 0.2" south and 1.5" west of the nucleus. This galaxy has a total magnitude of about 22.3. The 5 GHz radio map in Bridle et al. (1994) shows a large scale (LAS \sim 51") core, jet, double lobe source with the jet have an orientation of \approx 110°. The HST image shows a "finger" of extended emission in the counter-jet direction (PA \sim 300°).

3C 268.4, z=1.400

The image of 3C 268.4 does not appear to be extended in the EED analysis. PSF subtracting the image suggests that 3C 268.4 might be extended. In Figure 6, we show the possible resolved structure of the quasar. The HST image of 3C 268.4 reveals that it is another source with a complex morphology. The long axis (\approx 1.5") of the host is approximately along PA = 230°. In the faintest isophotes there is also a "finger" of emission pointing approximately to the south. In this direction there is a nearby (in projection) galaxy that is about 2.6" from the nucleus and has a total magnitude of 21.1. The 1.4 and 5 GHz radio images of Reid et al. (1995) show a core, jet, double lobe source with a largest angular size of about 12". The principal axis of the radio emission is approximately along PA = 215° and corresponds roughly to the principal axis of the host galaxy.

3C 270.1, z=1.519

According to the EED analysis, 3C 270.1 does not appear to be extended. However, in Figure 6, we show the morphology of the possible extended emission obtained by PSF subtraction which suggests that the image of 3C 270.1 is resolved. The host galaxy of 3C 270.1 is oriented preferentially in the east-west direction (PA=100°). There are "plumes" of emission to the south and to the north-west. The high resolution radio image of Akujor et al. (1994) shows a compact (LAS \sim 10"), "bent", triple source (core + two lobes) along PA \approx 180° and 320°.

3C 277.1, z=0.321

The host galaxy of 3C 277.1 is large compared to those in the rest of the sample (emission is seen over 3" down to $22 \text{ m}_{F702W} \text{ arcsec}^{-2}$). The overall morphology of the host is round, but distortions to the inner isophotes are seen in the directions of PA \approx 170° and 310°. The high resolution 1.7 and 5 GHz images of Reid et al. (1995) show a compact (LAS \sim 1.5") double oriented along PA \approx 310°. The position of the radio "hotspot" to the northwest roughly corresponds to the distortion we see in the HST image of the host galaxy.

$3C\ 279,\ z=0.538$

The image of this quasar was saturated. No PSF subtraction was attempted.

3C 280.1, z=1.659

The host galaxy of 3C 280.1 is compact and compared to most other hosts in the sample, its surface brightness increases rapidly with decreasing distance from the nucleus. The isophotes are round (e \sim 0.05) and are oriented along PA \approx 350°. The 5 GHz radio map of Swarup, Sinha, & Saika (1982; but see also Lonsdale et al. 1992 and Akujor et al. 1994) shows a core, two hotspots (one close to the nucleus, \sim 1" to the southeast, and a more distant one, about 12" to the west-northwest) and then a wiggly chain of emission to the southeast along PA \approx 120°. This "chain" of radio emission is seen from about 4" to about 11" from the nucleus. The host galaxy, as seen in our HST image, does have an outward bending of the isophotes along the direction of and over the region of the southeastern hotspot seen in the radio maps of Swarup et al. (1982).

3C 287, z=1.055

The HST data are not spatially resolved.

3C 288.1, z=0.961

The HST data are not spatially resolved.

3C 298, z=1.436

The host galaxy of 3C 298 is dominated by two morphological features — an "arm" of emission that projects from the nucleus to the south-west (PA=225°) and then bends around to the east and a "plume" of emission to the north-northeast of the nucleus (PA \approx 20°). The radio images of Rendong et al. (1991) and van Breugel et al. (1992) show a compact triple source (LAS \sim 1.8") with an east-west orientation.

3C 309.1, z=0.905

The host galaxy of 3C 309.1 is a flat elliptical galaxy. The major axis of the host galaxy is oriented along PA=130°. The high resolution radio image of Redong et al. (1991)

shows 3C 309.1 to be a compact source, with a nuclear region oriented along PA \approx 145° and a LAS \sim 0.1" and a "lobe" about 1" from the nucleus along PA \approx 95°. The highest surface brightness isophotes of the host have an orientation roughly like that of the nuclear radio emission.

3C 334, z=0.555

The HST image of 3C 334 shows a host galaxy that is distorted, having twisted and off-center isophotes. The general orientation of the host is $PA\approx120^{\circ}$ and is 1.5" across along its major axis (down to a surface brightness of $21~\mathrm{m}_{F702W}~\mathrm{arcsec}^{-2}$). The 5 GHz radio image of Bridle et al. (1994) shows a large (LAS ~57 ") triple (core, jet, two radio lobes) source. The radio jet emerges from the nucleus at $PA\approx140^{\circ}$ and curves around to the north. The orientation of the optical image of the host galaxy is approximately the same as that of the radio (5 GHz) image. Several ground-based images of 3C 334 show that it is extended and has a morphology similar to that presented here. For example, an $[OII]\lambda3727$ image in Hes et al. (1996) shows that 3C 334 is extended along $PA\approx10^{\circ}$ and a $[OIII]\lambda5007$ image of Lawrence (1990) shows extended line emission along $PA\approx150^{\circ}$. Both results have some morphological similarity to the image presented in this study.

3C 343, z=0.988

The image of 3C 343 is most unusual for the quasars imaged in this sample; it did not require any PSF subtraction! It appears to be a flat system with a major axis of about 2" long oriented along PA \approx 60°. 3C 343 is another CSS radio source. The radio map of Rendong et al. (1991) reveals a compact (LAS \approx 0.3") complex radio source. There is a finger of emission (a jet?) pointing out along PA \approx 320°. From an analysis of an optical spectrum, Aldcroft, Bechtold, & Elvis (1994) suggest that 3C 343 is a Seyfert 2 galaxy (i.e., the galaxy has narrow permitted and forbidden lines). Given the high radio luminosity of this galaxy, a more appropriate classification is as a radio galaxy. The characteristics of the optical spectrum from Aldcroft et al. supports our imaging data and our contention that 3C 343 does not appear to be a quasar.

3C 351.0, z=0.371

The image of this quasar was saturated. No PSF subtraction was attempted.

3C 380, z=0.692

3C 380 appears to be marginally resolved and is perhaps an interacting system. It has two companion galaxies that appear to be immersed in common isophotes with the host galaxy of 3C 380. These galaxies are approximately 0.6" west and 0.5" north and 0.8" west and 0.7" north of the nucleus respectively. The total magnitudes of these two galaxy are

 $m_{F702W} \approx 20.7$ and $m_{F702W} \approx 21.9$. The radio image of van Breugel et al. (1992) at 1.4 GHz shows a very diffuse radio morphology that is strikingly similar but larger than the optical HST image shown in Figure 5. The interacting companions are engulfed in this radio emission and there is a surface brightness enhancement of the radio emission over the area of these companions (Reid et al. 1995).

3C 418, z=1.686

3C 418 appears to have a compact host galaxy with several nearby (in projection) galaxies. The long axis of the host is only about 0.9" across (down to a surface brightness of $22.9~\mathrm{m}_{F702W}~\mathrm{arcsec}^{-2}$) and oriented preferentially along PA \approx 225°. The two nearby galaxies are 0.9"W, 0.2"N and 1.2"W, 1.2"N from the nucleus and have magnitudes of 23.8 and 23.0 m_{F702W} . A 15 GHz radio image of O'Dea, Barvainis, & Challis (1988) shows a complex radio morphology with several bends in a radio "jet" pointing approximately along PA=330°. This twisted jet is approximately 2" long. The positions of the bends in the radio jet seem to correspond roughly to the positions of these nearby "companions" seen in the PSF subtracted HST image. However, given the magnitudes of these "companions", it seems very unlikely that they would be at the redshift of the quasar.

3C 432, z=1.785

The HST data for 3C 432 are not extended according to the EED analysis. However, PSF subtraction suggests that 3C 432 may in fact be resolved. The HST image of 3C 432 shows a compact host about 1.2" in diameter down to a surface brightness of 22 m_{F702W} arcsec⁻². The host is preferentially oriented along PA \approx 45°. There is a secondary "plume" of emission along PA \approx 135°. A 4.9 GHz radio map of Bridle et al. (1994) shows a classical core, jet, double lobed source extended over 15" and oriented along PA \approx 135°.

3C 454, z=1.757

The HST image of 3C 454 reveals a round and compact (\sim 1" at a surface brightness of 22 m_{F702W} arcsec⁻²) host galaxy. The radio morphology is also compact, with a largest angular size of about 0.8" (Rendong et al. 1991; Spencer et al. 1991). The radio emission is oriented preferentially in the north-south direction (Spencer et al. 1991). As is the case for 3C 181 and 3C 288.1, we urge caution in interpreting several of the features in the PSF subtracted image shown in Figure 5. Some of the structure seen along PA \approx 205° may be due to incomplete removal of the most intense diffraction spike (i.e., the one in the +U3 direction). The questionable accuracy of the PSF removal is noted in Table 3.

3C 454.3, z=0.860

The image of this quasar was saturated. No PSF subtraction was attempted.

3C 455, z=0.5427

The image of 3C 455 is interesting. It has one of the highest extended/total brightness ratios of the entire sample (\sim 70%). It has a simple diffuse morphology with an embedded high surface brightness nucleus. Down to a surface brightness of about 22 mag arcsec⁻², 3C 455 is about 2" in diameter along its major axis at PA \approx 60°. The radio morphology in the 8 GHz map of Bogers et al. (1994) is a core, double radio lobe type oriented along PA \approx 245° (very similar to the optical major axis seen in the HST image). The spectrum of this object shown in Gelderman & Whittle (1994) shows narrow permitted lines. Combined with our result that very little point-source subtraction was necessary, suggests that this object should be re-classified as a compact radio galaxy rather than a quasar.

8. Concluding Remarks

We can draw some general conclusions from an analysis of the images presented in Figures 5 and 6. We present HST "snapshot" images of a sample of 43 quasars. From a close inspection and analysis of these data we draw the following conclusions:

- Our analysis suggests that the quasar fuzz contributes from <5% to nearly 100% in the most extreme case (about 20% being typical) of the total light from the quasar. Although a large fraction of the objects do not appear to be resolved in the EED analysis (\sim 40%), in about 1/2 of those sources, the more sensitive PSF subtraction indicates the presence of a resolved component.
- Many of the resolved sources show complex morphology with twisted, asymmetric, and/or distorted isophotes and irregular extensions.
- In almost every case of the quasars with spatially resolved "fuzz", there are similarities between the radio and optical morphologies. In many cases there are features with similar radio and optical morphologies and/or the principal axes of radio and optical (continuum and line) emission are roughly aligned. This is further evidence for the reality of the structures detected in the PSF analysis.
- •A significant fraction ($\sim 25\%$) of sources show galaxies nearby in project (within 5") and some ($\sim 10\%$ of the sources) show obvious signs of interactions with these nearby companions.

These results show that the generally complex morphologies of host galaxies of quasars are influenced by the radio emitting plasma and by the presence of nearby companions.

We must be cautious in interpreting these data since all of the images have a contribution

from emission lines to their morphologies and brightnesses. Separation of the continuum and line contributions and constraints on the various mechanisms involved await new snapshot surveys that are being carried out of 3C sources with the linear ramp filters and another broad-band filter. A more robust and quantitative analysis of the data and the relationship between high redshift radio galaxies and quasars will be presented in a future paper.

This research is partially supported by HST GO grant number GO-5476.01-93A, by a program funded by the Dutch Organization for Research (NWO) and by a NATO research grant. M. D. L. would like to thank Chris Burrows, Tim Heckman, and Matt McMaster for useful suggestions. We would also like to thank an anonymous referee for her/his remarks that improved the presentation of our results.

REFERENCES

- Akujor, C. E., Spencer, R. E., Zhang, F. J., Davis, R. J., Browne, I. W. A., & Fanti, C. 1991, MNRAS, 250, 215
- Akujor, C. E., Ludke, E., Browne, I. W. A., Leahy, J. P., Garrington, S. T., Jackson, N., & Thomasson, P. 1994, A&AS, 105, 247
- Aldcroft, T. L., Bechtold, J., & Elvis, M. 1994, ApJS, 93, 1
- Bahcall, J.N., Kirhakos, S., & Schneider, D.P. 1995a, ApJ, 450, 486
- Bahcall, J.N., Kirhakos, S., & Schneider, D.P. 1995b, ApJ, 447, L1
- Barthel, P. 1989, ApJ, 336, 606
- Baum, S. A., de Koff, S., Sparks, W. B., Golombek, D., Biretta, J., Macchetto, D., Miley, G. M., & Mc Carthy, P. J. 1999, in preparation
- Bennett, A. S. 1962a, Mem. RAS, 68, 163
- Bennett, A. S. 1962b, MNRAS, 125, 75
- Bogers, W. J., Hes, R., Barthel, P. D., & Zensus, J. A. 1994, A&AS, 105, 91
- Boyce, P. J. et al. 1998, MNRAS, 298, 121
- Boyce, P. J., Disney, M. J., & Bleaken, D. G. 1998, MNRAS, 302, L39
- Browne, I. W. A., Orr, M. J. L., Davis, R. J., Foley, A., Muxlow, T. W. B., & Thomasson, P. 1982, MNRAS, 198, 673
- Bridle, A. H., Hough, D. H., Lonsdale, C. J., Burns, J. O., & Laing, R. A 1994, AJ, 108, 766
- Chambers, K., Miley, G., & van Breugel, W. 1987, Nature, 329, 604
- de Koff, S., Baum, S. A., Sparks, W. B., Golombek, D., Biretta, J., Macchetto, D., McCarthy, P., & Miley, G. K. 1996, ApJS, 107, 621
- de Pater, I., & Perley, R. A. 1983, ApJ, 273, 64
- Disney, M.J. et al. 1995, Nature, 376, 150
- Djorgovski, S., Spinrad, H., Mc Carthy, P., et al. 1988, AJ, 96, 836

Fanti, C., Fanti, R., Parma, P., Venturi, T., Schilizzi, R. T., Rendong, N., Spencer, R. E., Muxlow, T. W. B., van Breugel, W. 1989, A&A, 217, 44

Gelderman, R., & Whittle, M. 1994, ApJS, 91, 491

Hartwick, F., & Schade, D. 1990, ARAA, 28, 437

Heckman, T. M., Lehnert, M. D., van Breugel, W. J. M., & Miley, G. K. 1991, ApJ, 370, 78

Hes, R., Barthel, P., & Fosbury, R. 1996, A&A, 313, 423

Hooper, E. J., Impey, C. D., & Foltz, C. B. 1997, ApJ, 480, L95

HST Data Handbook, Version 2, eds. C. Leitherer, STScI Publication, (December 1995)

Hutchings, J.B., & Morris, S.C. 1995, AJ, 109, 1541

Hutchings J. B., Crampton D., & Campbell B. 1984, ApJ, 280, 41

Lawrence, C. 1990, in Parsec Scale Radio Jets, eds. J. A. Zensus and T. J. Pearson, (Cambridge: Cambridge University Press), P. 294

Lehnert, M. D., van Breugel, W. J. M., Heckman, T. M., & Miley, G. K. 1999, ApJS accepted

Lonsdale, C. J., Barthel, P. D., & Miley, G. K. 1993, ApJS, 87, 63

Malkan, M. A. 1984, ApJ, 287, 555

McCarthy, P., van Breugel, W., Spinrad, H., & Djorgovski, S. 1987, ApJL, 321, L29

McCarthy, P., Miley, G. K., de Koff, S., Baum, S. A., Sparks, W. B., Golombek, D., Biretta, J., & Macchetto, D. 1997, ApJS, 112, 415

Mantovani, F., Junor, W., Fanti, R., Padrielli, L., Browne, I. W. A., & Muxlow, T. W. B. 1992, MNRAS, 257, 353

Neff, S., & Hutchings, J. 1990, AJ, 100, 1441

Norman, C., & Miley, G. K. 1984, A&A, 141, 85

O'Dea, C. P., Barvainis, R., & Challis, P. M. 1988, AJ, 96, 435

Price, R., Gower, A. C., Hutchings, J. B., Talon, S., Duncan, D., & Ross, G. 1993, ApJS, 86, 365

- Reid, A., Shone, D. L., Akujor, C. E., Browne, I. W. A., Murphy, D. W., Pedelty, J., Rudnick, L., & Walsh, D. 1995, A&AS, 110, 213
- Rendong, N., Schilizzi, R. T., Fanti, C., & Fanti, R. 1991, A&A, 252, 513
- Ridgway, S. E. & Stockton, A. 1997, AJ, 114, 511
- Sanghera, H. S., Saikia, D. J., Ludke, E., Spencer, R. E., Foulsham, P. A., Akujor, C. E., & Tzioumis, A. K. 1995, A&A, 295, 629
- Schilizzi, R. T., Kapahi, V. K., & Neff, S. G. 1982, JAp&A, 3, 173
- Schneider, D. P., van Gorkom, J. H., Schmidt, M., & Gunn, J. E. 1992, AJ, 103, 1451
- Smith, E. P., Heckman, T. M., Bothun, G., Romanishin, W., & Balick, B. 1986, ApJ, 306, 64
- Spencer, R. E., Schilizzi, R. T., Fanti, C., Fanti, R., Parma, P., van Breugel, W. J. M., Venturi, T., Muxlow, T. W. B., & Rendong, N. 1991, MNRAS, 250, 225
- Spinrad, H., Djorgovski, S., Marr, J., & Aguilar L. 1985, PASP, 97, 932
- Stockton A., & MacKenty, J. W. 1987, ApJ, 316, 584
- Swarup, G., Sinha, R. P., & Saikia, D. J. 1982, MNRAS, 201, 393
- van Breugel, W. J. M., Fanti, C., Fanti, R., Stanghellini, C., Schilizzi, R. T., & Spencer, R. E. 1992, A&A, 256, 56
- Veron-Cetty, M. -P., & Woltjer, L. 1990, A&A, 236, 69
- Wide Field and Planetary Camera 2 Instrument Handbook, C. J. Burrows (Ed.), STScI Publication (June 1995)
- Whitmore, B. 1995, in Calibrating Hubble Space Telescope: Post Servicing Mission, ed. A. Koratkar and C. Leitherer (Baltimore: Space Telescope Science Institute), p. 269

This preprint was prepared with the AAS IATEX macros v4.0.

FIGURE CAPTIONS

- Fig. 1.— The redshift distribution of the observed sample of quasars from the 3CR catalogue.
- Fig. 2.— The 178 MHz radio power distribution of the observed sample of 3CR quasars.
- Fig. 3.— The largest linear size distribution of the radio emission for the observed sample of 3CR quasars. We assumed a cosmology of $H_0=75 \text{ km s}^{-1} \text{ Mpc}^{-1}$ and $q_0=0.5$ in making this figure.
- Fig. 4.— The ratio of the QSO to PSF EEDs determined as described in the text. Those sources that have extended fractions above 1.05 are considered resolved. The uncertainties were determined assuming only that photon noise from quasar and PSF light profiles and sky background contribute to the uncertainties in the ratio (i.e., we neglect possible systematic effects).

Fig. 5.— a) Contour plots of PSF subtracted images of the quasars 3C 14 (z=1.469), 3C 43 (z=1.47), 3C 47 (z=0.425), and 3C 93 (z=0.357). The lowest contours in each plot are: $22.3 \text{ m}_{F702W} \text{ arcsec}^{-2} \text{ for 3C } 14, 22.9 \text{ m}_{F702W} \text{ arcsec}^{-2} \text{ for 3C } 43, 22.9$ 3C 47, and 22.9 m_{F702W} arcsec⁻² for 3C 93. As in every plot of this figure, each contour is an increase of a factor of 2 (0.75 magnitudes) in surface brightness and each image has been smoothed with a 4 pixel × 4 pixel median filter. b) Contour plots of PSF subtracted images of the quasars 3C 138 (z=0.759), 3C 147 (z=0.545), 3C 175 (z=0.768), and 3C 179 (z=0.856). The lowest contours in each plot are: $22.3 \text{ m}_{F702W} \text{ arcsec}^{-2}$ for 3C 138, 22.1 m_{F702W} arcsec⁻² for 3C 147, 22.1 m_{F702W} arcsec⁻² for 3C 175, and 22.9 m_{F702W} arcsec⁻² for 3C 179. c) Contour plots of PSF subtracted images of the quasars 3C 190 (z=1.195), 3C 204 (z=1.112), 3C 215 (z=0.412) and 3C 216 (z=0.67). The lowest contours in each plot are: $22.7 \text{ m}_{F702W} \text{ arcsec}^{-2} \text{ for 3C } 190, 22.7 \text{ m}_{F702W} \text{ arcsec}^{-2} \text{ for 3C } 204, 21.9 \text{ m}_{F702W} \text{ arcsec}^{-2}$ for 3C 215, 22.1 m_{F702W} arcsec⁻² for 3C 216. d) Contour plots of PSF subtracted images of the quasars 3C 249.1 (z=0.313), 3C 263 (z=0.646), 3C 277.1 (z=0.321), and 3C 280.1 (z=1.659). The lowest contours in each plot are: $21.7 \text{ m}_{F702W} \text{ arcsec}^{-2}$ for 3C 249.1, 20.6 m_{F702W} arcsec⁻² for 3C 263, 22.1 m_{F702W} arcsec⁻² for 3C 277.1, and 22.9 m_{F702W} arcsec⁻² for 3C 280.1. e) Contour plots of PSF subtracted images of the quasars 3C 298 (z=1.436), 3C 309.1 (z=0.905), 3C 334 (z=0.555), and 3C 343 (z=0.988). The lowest contours in each plot are: $21.1 \text{ m}_{F702W} \text{ arcsec}^{-2} \text{ for 3C } 298, 21.9 \text{ m}_{F702W} \text{ arcsec}^{-2} \text{ for 3C } 309.1, 21.1 \text{ m}_{F702W}$ $arcsec^{-2}$ for 3C 334, 22.7 m_{F702W} $arcsec^{-2}$ for 3C 343. f) Contour plots of PSF subtracted images of the quasars 3C 380 (z=0.692), 3C 418 (z=1.686), 3C 454 (z=1.757), and 3C 455 (z=0.5427). The lowest contours in each plot are: $21.9 \text{ m}_{F702W} \text{ arcsec}^{-2}$ for 3C 380, 22.9 $m_{F702W} \ arcsec^{-2} \ for \ 3C \ 418, \ 22.3 \ m_{F702W} \ arcsec^{-2} \ for \ 3C \ 454 \ and \ 21.4 \ m_{F702W} \ arcsec^{-2} \ for \ 3C \ 454 \ arcsec^{-2} \ for$ 3C 455.

Fig. 6.— a) Contour plots of PSF subtracted that are not resolved according to the EED analysis (see text for details), but might be resolved as shown by PSF subtraction. The images of the quasars 3C 154 (z=0.58), 3C 186 (z=1.063), 3C 191 (z=1.956), and 3C 207 (z=0.684) are shown. The lowest contours in each plot are: 22.0 m_{F702W} arcsec⁻² for 3C 154, 22.4 m_{F702W} arcsec⁻² for 3C 186, 22.7 m_{F702W} arcsec⁻² for 3C 191, and 21.9 m_{F702W} arcsec⁻² for 3C 207. As in every plot of this figure, each contour is an increase of a factor of 2 (0.75 magnitudes) in surface brightness and each image has been smoothed with a 4 pixel × 4 pixel median filter. b) Contour plots of PSF subtracted images of the quasars 3C 254 (z=0.734), 3C 268.4 (z=1.4), 3C 270.1 (z=1.519) and 3C 432 (z=1.785). The lowest contours in each plot are: 21.9 m_{F702W} arcsec⁻² for 3C 254, 22.1 m_{F702W} arcsec⁻² for 3C 268.4, 22.7 m_{F702W} arcsec⁻² for 3C 270.1, and 22.4 m_{F702W} arcsec⁻² for 3C 432.

Fig. 7.— Histogram of the difference between the position angles of the principal axis of the radio and optical emission.

Table 1. Observation Log for 3CR Quasars

3CR (1)	N (2)	Int (3)	Date (4)	3CR (5)	N (6)	Int (7)	Date (8)
9.0	4	140	05/22/94	249.1	2	140	04/16/94
14.0	2	300	06/20/94	254.0	2	140	01/19/95
43.0	2	300	07/19/94	263.0	2	140	03/27/94
47.0	2	140	01/17/95	268.4	4	140	03/26/94
68.1	2	300	08/17/94	270.1	2	300	12/14/94
93.0	2	140	02/15/94	277.1	2	140	12/01/94
138.0	1	140	11/10/94	279.0	2	300	02/23/94
147.0	2	140	04/27/94	280.1	2	300	05/01/94
154.0	2	140	03/18/94	287.0	4	140	03/05/94
175.0	2	140	05/03/95	288.1	2	140	04/06/94
179.0	2	300	04/16/94	298.0	4	140	07/15/94
181.0	2	300	04/06/94	309.1	2	140	06/21/94
186.0	4	140	03/09/94	334.0	2	140	01/23/95
190.0	2	300	04/17/94	343.0	1	300	01/11/95
191.0	2	300	03/18/94	351.0	2	140	07/25/94
204.0	4	140	02/16/94	380.0	2	140	09/14/94
205.0	4	140	04/18/94	418.0	2	300	06/20/94
207.0	2	140	06/08/94	432.0	4	140	07/21/94
208.0	4	140	04/04/94	454.0	4	140	05/01/94
215.0	2	140	04/22/94	454.3	2	140	12/13/94
216.0	2	140	05/11/95	455.0	1	300	08/22/94
220.2	2	300	12/17/94				

Note. — Col. (1) and (5) — 3CR source designation. Col. (2) and (6) — Number of separate exposures each with the exposure time in listed in Col. (3) and (7) respectively. The total integration time is given by multiplying colums (2) and (3) or colums (6) and (7). Col. (3) and (7) — Integration time in seconds per exposure. Col. (4) and (8) — Date of observation. The two exposures for 3C179.0 and 3C279.0 were taken on different dates. For 3C179.0, the dates of the two exposures were 04/16/94 and 05/16/95, for 3C279.0, the dates are 02/23/94 and 05/20/95.

Table 2. Basic Properties of the 3CR Snapshot Survey Quasars

0.CD		7.7	0(170)	1 D		CI.	T A C	D.A.	IDC (1)	C
3CR	Z (2)	V (2)	S(178)	$\log P_{178}$	α	Class	LAS	PA	LPS (kpc)	ref
(1)	(2)	(3)	(4)	(5)	(6)	(7)	(8)	(9)	(10)	(11)
9	2.012	18.21	17.8	28.9	1.09	S	14	140	1.88	4,5
14	1.469	20	10.4	28.4	0.81	\mathbf{S}	26	355	2.17	1,2
43	1.47	20	11.6	28.5	0.75	\mathbf{C}	2.6	160	1.17	9,10
47	0.425	18.1	26.4	27.9	0.98	\mathbf{S}	85	215	2.57	4,6
68.1	1.238	19.5	12.8	28.4	0.80	\mathbf{S}	53	175	2.48	4
93	0.358	18.09	14.4	27.5	0.82	\mathbf{S}	41	40	2.22	3,6
138	0.759	17.9	22.2	28.2	0.46	\mathbf{C}	0.6	70	0.51	6,8,12
147	0.545	16.9	60.5	28.4	0.46	\mathbf{C}	0.8	240	0.59	3,12
154	0.5804	18	23.1	28.1	0.77	\mathbf{S}	53	100	2.42	3
175	0.768	16.6	17.6	28.2	0.98	\mathbf{S}	56	240	2.48	3,4
179	0.846	18.0	9.4	28.0	0.71	\mathbf{S}	18	270	2.00	7
181	1.382	18.92	14.5	28.5	1.00	\mathbf{S}	7.5	120	1.63	16
186	1.063	17.6	14.1	28.3	1.15	\mathbf{C}	2.5	140	1.15	8,10
190	1.197	20	15.0	28.4	0.93	\mathbf{C}	3	30	1.23	8,10,12
191	1.956	18.65	13.0	28.7	0.98	\mathbf{S}	5.2	165	1.45	1,2
204	1.112	18.21	10.5	28.2	1.08	\mathbf{S}	38	275	2.33	4,7
205	1.534	17.62	12.6	28.5	0.88	\mathbf{S}	19	20	2.03	7
207	0.684	18.15	13.6	28.0	0.90	\mathbf{S}	11	90	1.76	3
208	1.11	17.42	16.8	28.4	0.96	\mathbf{S}	15	265	1.93	1,2,4
215	0.411	18.27	11.4	27.5	1.06	\mathbf{S}	60	325	2.41	4,6
216	0.67	18.48	20.2	28.1	0.84	\mathbf{S}	6	40	1.49	7
220.2	1.157	19	7.2	28.1	0.61	\mathbf{S}	9	45	1.71	17
249.1	0.311	15.72	10.7	27.2	0.81	\mathbf{S}	27	100	2.00	3,4
254	0.734	17.98	19.9	28.2	0.96	\mathbf{S}	15	110	1.90	7
263	0.646	16.32	15.2	28.0	0.82	\mathbf{S}	51	110	2.42	4
268.4	1.4	18.42	10.3	28.4	0.80	\mathbf{S}	12	215	1.83	7
270.1	1.519	18.61	13.6	28.6	0.75	\mathbf{S}	10	175	1.75	2
277.1	0.32	17.93	8.5	27.2	0.64	\mathbf{C}	1.5	310	0.75	7
279	0.536	17.77	23.2	28.0	0.31	\mathbf{F}	5	205	1.38	2,18
280.1	1.659	19.44	9.2	28.4	0.93	\mathbf{S}	24	130	2.13	2,5,11
287	1.055	17.67	16.3	28.4	0.42	F	0.2	45	0.05	8,14
288.1	0.961	18.12	9.0	28.0	0.84	\mathbf{S}	7	265	1.59	2
298	1.439	16.79	47.5	29.1	0.99	\mathbf{C}	1.8	90	1.01	8,12
309.1	0.904	16.78	22.7	28.4	0.53	F	1.0	145	0.75	8

Table 2—Continued

3CR (1)	z (2)	V (3)	S(178) (4)	$\log P_{178} $ (5)	α (6)	Class (7)	LAS (8)	PA (9)	LPS (kpc) (10)	ref (11)
334	0.555	16.41	10.9	27.7	0.86	S	57	140	2.45	4
343	0.988	20.61	12.4	28.2	0.37	\mathbf{F}	0.3	320	0.23	8
351	0.371	15.28	13.7	27.5	0.73	\mathbf{S}	59	35	2.38	7
380	0.691	16.81	59.4	28.6	0.71	\mathbf{C}	1.5	315	0.90	3,7,12
418	1.686	20	13.1	28.6	0.44	\mathbf{F}	2.5	330	1.14	13
432	1.805	17.96	11.0	28.6	0.98	\mathbf{S}	15	135	1.92	4
454	1.757	18.47	11.6	28.6	0.90	\mathbf{C}	0.9	180	0.70	8,10
454.3	0.86	16.1	13.0	28.1	0.04	\mathbf{F}	5	310	1.44	15
455	0.5427	19.7	12.8	27.8	0.71	C/S	4.4	245	1.33	3

Note. — Col. (1) — 3CR source designation. Col. (2) — Redshift of the source as taken from Spinrad et al. (1986). Col. (3) — The V magnitude of the quasar taken from Spinrad et al. (1986). Col. (4) — The 178 MHz flux density of the quasar taken from Spinrad et al. (1986). Col. (5) — The logarithm of the 178 MHz power in Watts assuming the cosmology $q_0=0.5$ and $H_0=75$ km s⁻¹ Mpc⁻¹. Col. (6) — The spectral index of the radio emission as taken from Spinrad et al. (1986). Col. (7) — The classification of the radio source morphology and spectral index. Quasars classified as "S" are steep spectrum sources with spectral indices greater than 0.7 (Col. 6) and largest projected sizes greater than 20 kpc (Col. 10). Quasars classified as "C" are compact steep spectrum sources (CSS) or gigahertz peaked sources (GPS) and are sources with spectral indices greater than 0.7 (Col. 6) and largest projected sizes less than 20 kpc. Quasars classified as "F" are flat spectrum sources with spectral indices less than 0.7 (Col. 6). Col. (8) — The largest angular scale (LAS) in units of arc seconds of the radio emission as measured from the radio maps in the references given in Col. (11). Col. (9) — The position angle of the jet as measured relative to the core measured from the radio maps in the references given in Col. (11). In the few cases where a jet was not obvious, the position angle has been measured from the core through the brightest hotspot. The typical uncertainty in this determination is about $\pm 10^{\circ}$. Col. (10) — The largest projected physical size of the radio source determined using the largest angular scale from Col. (8) and the cosmology $q_0=0.5$ and $H_0=75$ km s⁻¹ Mpc⁻¹. The unit is the logarithm of the largest physical size in kpc. Col. (11) — The reference for the radio map used to measure the properties tabulated in Cols. (8) and (9). The references are 1 = Akujor et al. (1991), 2 = Akujor et al. (1994), 3 = Bogers et al. (1994), 4 = Bridleet al. (1994), 5 = Lonsdale et al. (1993), 6 = Price et al. (1993), 7 = Reid et al. (1995), 8 = Rendong et al. (1991), 9 = Sanghera et al. (1995), 10 = Spencer et al. (1991), 11 =Swarup et al. (1982), 12 = van Breugel et al. (1992), 13 = O'Dea et al. (1988), 14 = Fantiet al. (1989), 15 = Browne et al. (1982), 16 = Mantovani et al. (1994), 17 = Schilizzi,

Table 3. HST Results on 3CR Snapshot Survey Quasars

3CR	m_{total}	$\frac{resolved}{total}(EED)$	$\frac{resolved}{total}(PSF)$	Rot	μ_{lim}	Resolved	PA	O-R	Comments
(1)	(2)	(3)	(4)	(5)	(6)	(7)	(8)	(9)	(10)
		. ,	. ,						
9	17.3	< 0.05				N		?	
14	18.8	0.17	0.40	-65.0	22.3	Y	310	R	5
43	20.5	0.17	0.49	-66.7	22.9	Y	170	R?	6
47	17.7	0.17	0.38	113.6	22.9	Y	240	R	5
68.1	18.6	< 0.05	•••			N		?	•••
93	18.1	0.33	0.56	122.3	22.9	Y	170	R?	5
138	18.4	0.14	0.34	-39.0	22.3	Y	105	\mathbf{R}	5
147	17.2	0.08	0.39	112.5	22.1	Y	250	\mathbf{R}	5
154	16.9	< 0.05	0.17	136.6	22.0	Y?	170	N	6
175	<16.4	0.05	< 0.20	146.6	22.1	Y	230	R	1,3,7
179	18.5	0.12	0.38	136.7	22.9	Y	260	R	$3,\!5$
181	18.3	< 0.05				N		?	
186	17.5	< 0.05	0.32	155.8	22.4	Y?	140	R	5
190	18.9	0.07	0.28	146.4	22.7	Y	90	R?	6
191	17.8	< 0.05	0.36	140.7	22.7	Y?	210	N	3,5
204	17.8	0.05	0.18	-159.2	22.7	Y	330	N	5
205						N		?	2
207	17.5	< 0.05	0.34	153.6	21.9	Y?	90	R	3,5
208	18.2	< 0.05	•••			N		?	•••
215	17.7	0.14	0.40	151.6	21.9	Y	310	R	5
216	18.7	0.25	0.59	147.5	22.1	Y	30	R	5
220.2	<17.7	< 0.05	•••			N		?	
249.1	<15.8	0.20	< 0.73	-173.0	21.7	Y	120	R?	1,3,5
254	17.4	< 0.05	0.32	-57.1	21.9	Y?	100	R	5
263	15.9	0.14	0.11	-146.8	20.6	Y	160	N	3,7
268.4	17.3	< 0.05	0.29	-139.6	22.1	Y?	230	R	5
270.1	<18.0	< 0.05	< 0.35	-18.5	22.7	Y?	90	N	1,3,5
277.1	17.6	0.27	0.56	-3.9	22.1	Y	310	R	5
279		•••	•••			N		?	2
280.1	18.4	0.12	0.41	-150.4	22.9	Y	175	N	3,5
287	17.5	< 0.05	•••			N		?	•••
288.1	17.4	< 0.05	•••			N		?	•••
298	<16.4	0.10	< 0.18	155.4	21.1	Y	135	N	1,6
309.1	17.1	0.07	0.32	-176.6	21.9	Y	120	N	3,5
			-		-		-		, -

Table 3—Continued

3CR (1)	m_{total} (2)	$\frac{resolved}{total}$ (EED) (3)	$\frac{resolved}{total}(PSF-)$ (4)	Rot (5)	μ_{lim} (6)	Resolved (7)	PA (8)	O-R (9)	Comments (10)
334	<16.4	0.13	< 0.21	-15.9	21.1	Y	140	R	1,3,6
343	20.0	0.81	1.00	4.3	22.7	Y	80	R	5
351						N		?	2
380	16.9	0.05	0.36	148.5	21.9	Y	310	R	$3,\!5$
418	19.6	0.07	0.43	-98.6	22.9	Y	45	N	6
432	17.8	< 0.05	0.33	-106.4	22.4	Y?	200	N	3,5
454	18.4	0.18	0.49	-50.6	22.3	Y	140	N	4(206),6
454.3						N		?	2
455	18.8	0.21	0.69	-109.2	21.4	Y	240	R	5

Col. (1) — 3CR source designation. Col. (2) — Total magnitude within an aperture of radius 1.4 arc seconds. Col. (3) — The resolved fraction of the total emission within a 1.4 arc second aperture measured using the EED analysis. See text for details. Col. (4) — The resolved fraction of the total emission within a 1.4 arc second aperture measured by conducting PSF subtraction. See text for details. For those sources where the nucleus is saturated, we have given the measured resolved fraction as an upper limit. Col. (5) — Angle (in degrees) that the image was rotated to make north at the top and east to the left in each image. Positive values imply a counter-clockwise direction of the rotation. To calculate the PA of the brightest diffraction spike one uses the following formula: If the rotation angle is positive, then one subtracts 45° from the listed rotation angle. If the rotation angle is negative, then one adds 315° to the listed rotation angle. Possible residuals due to the diffraction spikes are noted in individual source descriptions in §7 and in Col. (10) of this table. Col. (6) — Surface brightness limit of the lowest contour of the plots shown in Figure 5 and 6 in units of magnitudes $\operatorname{arcsec}^{-2}$. Col. (7) — Is the quasar image resolved? "Y" implies that both the EED and PSF subtraction analyses suggest that the quasar image is resolved. "Y?" implies that only the PSF subtraction analysis suggests that the quasar image is resolved. "N" implies that the image is not resolved according to both analyses. Col. (8) — Position angle of the principal axis of the host galaxy measured north through east. The typical uncertainty is this determination is about $\pm 20^{\circ}$ (see §6 for details). Col. (9) — Is there an association between the radio and optical morphologies? A "R" implies that (i) the principal axis of the radio emission is within 20° of the principal axis of the optical emission or (ii) that there is a detailed correspondence between the morphological features seen in both the radio and optical. "R?" implies that there is some similarity in the optical and radio morphologies which may indicate a relationship between the radio and optical emission. "N" implies that there is little or no correspondence between the radio and optical emission. Col. (10) — Comments. A "1" implies that the nucleus is saturated and that PSF subtraction was attempted. A "2" implies that the nucleus was very saturated and that PSF subtraction was not attempted due to the severe saturation of the nucleus and the large angular scales over which the diffraction spikes are seen due to the nuclear point source. A "3" implies that the image has had a residual of the diffraction spike in the "+U3" direction removed by fitting a surface to the surrounding background (see text for details). A "4" implies that there is a possible residual in the displayed image due to the diffraction spike in the "+U3" direction. The number in parentheses after the "4" is the approximate position angle (measured relative to north through east) of the possible residual. A "5", "6", or "7" is used to characterize the level of uncertainty in the magnitude of the host galaxy due to the PSF subtraction. A "5" implies that the uncertainty in the magnitude of the host galaxy is about ± 0.2 magnitudes. A "6" implies that the uncertainty in the magnitude of the host galaxy is about ± 0.4 magnitudes. A "7" implies that the uncertainty in the magnitude of the host galaxy is about ± 0.7 magnitudes.

This figure "fig1.gif" is available in "gif" format from:

This figure "fig2.gif" is available in "gif" format from:

This figure "fig3.gif" is available in "gif" format from:

This figure "fig4a.gif" is available in "gif" format from:

This figure "fig4b.gif" is available in "gif" format from:

This figure "fig4c.gif" is available in "gif" format from:

This figure "fig4d.gif" is available in "gif" format from:

This figure "fig4e.gif" is available in "gif" format from:

This figure "fig4f.gif" is available in "gif" format from:

This figure "fig4g.gif" is available in "gif" format from:

This figure "fig5a.gif" is available in "gif" format from:

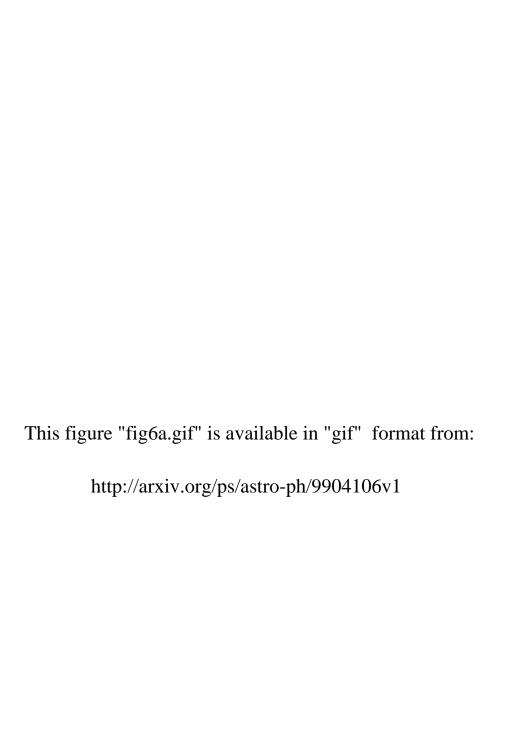
This figure "fig5b.gif" is available in "gif" format from:

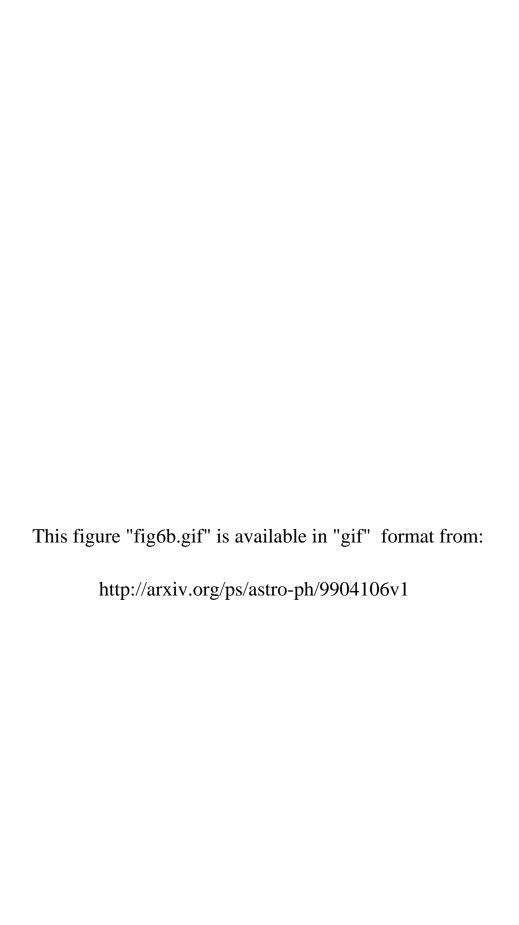
This figure "fig5c.gif" is available in "gif" format from:

This figure "fig5d.gif" is available in "gif" format from:

This figure "fig5e.gif" is available in "gif" format from:

This figure "fig5f.gif" is available in "gif" format from:





This figure "fig7.gif" is available in "gif" format from: